J. theor. Biol. (2002) **219,** 137–152
doi:10.1006/yjtbi.3077, available online at http://www.idealibrary.com on IDEAL®

Axisymmetric Bioconvection in a Cylinder

S. GHORAI*† AND N. A. HILL‡

†*Department of Mathematics, Indian Institute of Technology, Kanpur* 208016, *India and*
‡*Department of Mathematics, University of Glasgow, Glasgow G*12 8*QW, U.K.*

(*Received on* 11 *October* 2001, *Accepted in revised form on* 3 *May* 2002)

In three-dimensional bioconvection, the regions of rising and sinking fluid are dissimilar. This geometrical effect is studied for axisymmetric bioconvection in a cylindrical cell with stress-free (i.e. normal velocity and tangential stress vanish) lateral and top boundaries, and rigid bottom boundary. Using the continuum model of Pedley *et al.* (1988, *J. Fluid Mech.***195,** 223–237) for bioconvection in a suspension of swimming, gyrotactic microorganisms, the structure and stability of an axisymmetric plume in a deep chamber are investigated. The system is governed by the Navier–Stokes equations for an incompressible fluid coupled with a microorganism conservation equation. These equations are solved numerically using a conservative finite-difference scheme. Comparisons are made with two-dimensional bioconvection.

1. Introduction

Bioconvection is the term used to describe the phenomenon of spontaneous pattern formation in suspensions of microorganisms such as bacteria and algae (Pedley & Kessler, 1992). In all cases, the microorganisms are up to 10% denser than water and on average they swim upwards (although the reasons for up swimming may be different for different species). Microorganisms respond to certain stimuli by swimming, on average, in particular directions. These responses are called *taxes*, examples being *gravitaxis, phototaxis* and *gyrotaxis*. *Gravitaxis* indicates swimming opposite to gravity, whereas *phototaxis* denotes swimming towards or away from light. *Gyrotaxis* is swimming directed by the balance of torques due to gravity acting on a bottom-heavy cell and shear flow. We consider gyrotaxis in this paper.

*Tel.: +91-512-597-636; fax: +91-512-597-500.
E-mail address: sghorai@iitk.ac.in (S. Ghorai).

Cells swim randomly but, for example, if a neutrally buoyant cell is bottom-heavy (i.e. its centre of gravity is posterior to its centre of buoyancy), the cell will tend to swim vertically upwards in the absence of any other stimuli resulting in gravitaxis (Kessler, 1985). Such cells are also gyrotactic in that a local velocity gradient will produce viscous torques on the cell's body tending to tip it away from the vertical. If the cells do tend to swim upwards, the top layer of the suspension becomes denser than the layer below. When the governing parameters are above critical values, this leads to convective instability and formation of convection patterns. This phenomenon is known as ''bioconvection'', it has some similarity with Rayleigh–Bénard convection, but is driven solely by the swimming of the microorganisms.

For simplicity, algal cells such as *Chlamydomonas* (whose shapes closely approximate a spheroid) are idealized here as spheres of radius a. Let the unit vector $\mathbf{p}$ point in the swimming

0022-5193/02/$35.00/0

direction of the cell. The torque balance equation leads to the following equation for the reorientation rate (Hinch & Leal, 1972);

$$\dot{\mathbf{p}} = \frac{1}{2B}\left[\mathbf{k} - (\mathbf{k}\cdot\mathbf{p})\,\mathbf{p}\right] + \frac{1}{2}\boldsymbol{\omega}\wedge\mathbf{p}, \qquad (1)$$

where $\mathbf{k}$ points opposite to gravity, $\boldsymbol{\omega}$ is the vorticity, and B is the gyrotactic orientation parameter. The unit vector $\mathbf{p}$ is specified by Euler angles θ, ϕ so that

$$\mathbf{p} = (\sin\theta\cos\phi,\ \sin\theta\sin\phi,\ \cos\theta)$$

referred to axes through the geometric centre of the cell. Simplification of eqn (1) gives

$$\frac{\mathrm{d}\theta}{\mathrm{d}t} = -\frac{\sin\theta}{2B} + \frac{\zeta}{2}, \qquad (2)$$

where $\zeta = \boldsymbol{\omega}_{\phi}$ is the horizontal vorticity component.

Previous numerical studies of bioconvection were carried out in two dimensions only. Harashima *et al.* (1988) solved the equations of bioconvection numerically for purely up-swimming cells (i.e. $\theta = 0$) in a two-dimensional layer of finite depth and width, and studied the evolution of bioconvection from an initially uniform state. They proposed *minimum potential energy* as a principle for determining the steady-state roll size for a given value of Rayleigh number and a given box size. Their computational domain had a width/height ratio of 8. In contrast, Ghorai & Hill (1999, 2000a) investigated the stability of a two-dimensional gyrotactic plume in deep chambers. The top and the bottom of the chambers were stress free and rigid, respectively. In one study (Ghorai & Hill, 1999), the side walls were stress free and, in the other case (Ghorai & Hill, 2000a), they were periodic. In deep chambers, the meandering instability always dominates the varicose instability for stress-free side walls, but either can be dominant for periodic side walls, depending on the parameter values. Ghorai & Hill (2000b) also investigated the horizontal wavelengths of the gyrotactic plumes in wide chambers. Here, the steady-state wavelength, in contrast to Harashima *et al.* (1988), is not determined by the minimum potential energy. Recently, Hopkins & Fauci (2002) simulated two-dimensional bioconvection using point particles rather than a continuum model and examined the general effects of a variety of different responses by the microorganisms, including gyrotaxis and chemotaxis, although they did not make specific comparisons with any particular biological system.

Although it is easy to solve the two-dimensional problem, bioconvection is intrinsically three dimensional. The bioconvection pattern, for example, has polygonal cells (e.g. squares, pentagons and hexagons) each with a narrow descending central core surrounded by a broad column of rising fluid. Rayleigh (1916) noted that we may regard the hexagon "as deviating comparatively little from the circular form". The work by Rayleigh was an attempt to examine theoretically the results of the Beńard's experiment on a layer of fluid heated from below. In contrast to bioconvection, fluid in Rayleigh–Bénard convection rises along the central core and descends at the boundary between a polygonal cell and its neighbours. Axisymmetric convection in a cylindrical cell provides the simplest three-dimensional configuration: if fluid rises along the perimeter and sinks along the central axis, there is an asymmetry between the upward and downward moving regions. On the other hand, bioconvection in two dimensions assumes the cells to be infinitely long rolls where fluid ascends and descends along infinite parallel horizontal lines. This differs from the experimental findings where polygonal cells were observed. We have therefore investigated axisymmetric bioconvection confined between stress-free sidewalls, on which the normal velocity and tangential stress vanish.

2. Mathematical Formulation

Consider the motion of a viscous suspension of fluid within a vertical cylinder of height H and diameter L. As in Pedley *et al.* (1988), we assume that a monodisperse cell population can be modelled by a continuous distribution. Each cell has a volume ϑ and density $\rho + \delta\rho$, where ρ is the constant density of water in which the cells swim, and $\delta\rho \ll \rho$. The suspension is dilute, so that the volume fraction of the cells is small and cell–cell interactions are negligible.

2.1. GOVERNING EQUATIONS

We adopt cylindrical polar coordinates (r, ϕ, z) with the z-axis vertical. For axisymmetric bioconvection, we constrain the flow to be independent of the azimuthal angle ϕ. Then

$$\mathbf{u} = (u, 0, v), \qquad \boldsymbol{\omega} = (0, \zeta, 0) \tag{3}$$

and, from the continuity equation, we introduce stream function ψ such that

$$\mathbf{u} = \frac{1}{r}\left(-\frac{\partial\psi}{\partial z}, 0, \frac{\partial\psi}{\partial r}\right). \tag{4}$$

Conservation of cells requires that the number of cells per unit volume, $n(r, z, t)$, satisfies the equation

$$\frac{\partial n}{\partial t} = -\boldsymbol{\nabla}\cdot\mathbf{J}, \tag{5}$$

where the flux of the cells is

$$\mathbf{J} = (\mathbf{u} + W_c\bar{\mathbf{p}})\, n - D\,\boldsymbol{\nabla} n. \tag{6}$$

The third term in eqn (6) represents the random component of the cell locomotion. The diffusion coefficient D is assumed to be homogeneous, isotropic and independent of the other parameters of the problem. The second term in eqn (6) arises due to the average swimming of the cells: $W_c\bar{\mathbf{p}}$ is the average swimming velocity relative to the fluid and W_c is assumed to be constant. Here, $\bar{\mathbf{p}}$ represents the average orientation of the cells.

The vorticity evolves according to the equation

$$\frac{\partial\zeta}{\partial t} + \frac{\partial}{\partial r}(u\zeta) + \frac{\partial}{\partial z}(v\zeta) = \nu\left[\frac{\partial}{\partial r}\left\{\frac{1}{r}\frac{\partial}{\partial r}(r\zeta)\right\} + \frac{\partial^2\zeta}{\partial z^2}\right] + \frac{g\,\vartheta\,\delta\rho}{\rho}\frac{\partial n}{\partial r}, \tag{7}$$

where ν is the kinematic viscosity. Equation (7) is derived under the Boussinesq approximation, neglecting all effects of the cells on the fluid, except their negative buoyancy, because the suspension is dilute.

The equations are scaled using the diameter L, the time scale L^2/D and the mean concentration $\bar{n}$. The resulting system of coupled equations is

$$\mathbf{u} = \left(-\frac{1}{r}\frac{\partial\psi}{\partial z}, 0, \frac{1}{r}\frac{\partial\psi}{\partial r}\right),$$

$$-\zeta = \frac{1}{r}\frac{\partial^2\psi}{\partial z^2} + \frac{\partial}{\partial r}\left(\frac{1}{r}\frac{\partial\psi}{\partial r}\right), \tag{8}$$

$$\frac{\partial\zeta}{\partial t} + \frac{\partial}{\partial r}(u\zeta) + \frac{\partial}{\partial z}(v\zeta) = S_c\left[\frac{\partial}{\partial r}\left\{\frac{1}{r}\frac{\partial}{\partial r}(r\zeta)\right\} + \frac{\partial^2\zeta}{\partial z^2}\right] + S_c\,R\frac{\partial n}{\partial r} \tag{9}$$

and

$$\frac{\partial n}{\partial t} + \frac{1}{r}\frac{\partial}{\partial r}\left[r\left\{(u + V_c\,\bar{p}_r)n - \frac{\partial n}{\partial r}\right\}\right] + \frac{\partial}{\partial z}\left[(v + V_c\,\bar{p}_z)n - \frac{\partial n}{\partial z}\right] = 0. \tag{10}$$

For convenience, we have kept the same notation for dimensional and dimensionless variables. Here, $S_c = \nu/D$ is the Schmidt number, $V_c = W_c\,L/D$ is the scaled swimming speed and R is a Rayleigh number defined as

$$R = \frac{\vartheta\,\delta\rho\,g\,\bar{n}\,L^3}{\rho\,\nu D}.$$

The definition of R is non-standard in that it is based on the width rather than the height of the chamber. The conventional Rayleigh number increases with an increase in the height of the chamber, whereas ours remains constant. We use our definition so that the height of the chamber can be varied independently of the other parameters. The boundary conditions are applied at

$$r = 0, 1/2 \quad \text{and} \quad z = 0, \lambda,$$

where $\lambda = H/L$ is the aspect ratio of the chamber.

The values of the non-dimensional numbers are calculated from the estimates of typical parameters given in Table 1 (Kessler, 1986). However, the non-dimensional numbers are sensitive to the estimated parameter values.

2.2. CALCULATION OF THE MEAN DIRECTION

The unit vector $\mathbf{p}$ in the direction of swimming is given by

$$\mathbf{p} = (p_r, p_z) = (\sin\theta, \cos\theta),$$

where θ is the solution of eqn (2).

TABLE 1
Estimates of typical parameters for a suspension of alga C. nivalis (Kessler, 1986)

Cell radius	a	10^{-3} cm
Cell volume	ϑ	5×10^{-10} cm^3
Cell density ratio	$\delta\rho/\rho$	5×10^{-2}
Cell diffusivity	D	5×10^{-4} cm^2 s^{-1}
Gyrotactic parameter	B	≈ 3.4 s
Swimming speed	W_c	10^{-2} cm s^{-1}
Mean concentration	$\bar{n}$	10^6 cm^{-3}
Kinematic viscosity	ν	10^{-2} cm^2 s^{-1}

If the shear is sufficiently small so that $|B\zeta| \leqslant 1$, then the steady-state orientation is obtained by setting the left-hand side of eqn (2) equal to zero. When $|B\zeta| \leqslant 1$, we find that

$$\bar{\mathbf{p}} = (\bar{p}_r, \bar{p}_z) = \left(\beta, [1 - \beta^2]^{1/2}\right), \quad |\beta| \leqslant 1, \quad (11)$$

where $\beta = B\zeta$. If the vorticity is large ($|B\zeta| > 1$), the cell tumbles but swims on average in a fixed direction to the vertical. In this case, the swimming direction $\mathbf{p}$ is approximated by integrating the swimming direction over the tumbling period (Ghorai & Hill, 1999). If $\beta = B\zeta > 1$, then

$$\bar{\mathbf{p}} = (\bar{p}_r, \bar{p}_z) = \left(\beta - [\beta^2 - 1]^{1/2}, 0\right) \quad (12)$$

and similarly, if $\beta = B\zeta < -1$, then

$$\bar{\mathbf{p}} = (\bar{p}_r, \bar{p}_z) = \left(\beta + [\beta^2 - 1]^{1/2}, 0\right). \quad (13)$$

Equations (11)–(13) determine the average swimming direction of the cells for any value of ζ. After scaling, $\beta = G\zeta$, where $G = BD/L^2$ is the dimensionless gyrotaxis number, which represents the ratio of the reorientation time due to gyrotaxis to the diffusion time.

2.3. INITIAL AND BOUNDARY CONDITIONS

We impose rigid, no-slip boundary conditions at the bottom wall and assume that the other boundaries are stress free, so that

$$\psi = 0 \quad \text{at } r = 0, 1/2 \quad \text{and} \quad z = 0, \lambda, \quad (14a)$$

$$\frac{\partial \psi}{\partial z} = 0 \quad \text{at } z = 0 \quad (14b)$$

$$\zeta = 0 \quad \text{at } z = \lambda \quad \text{and} \quad r = 0, 1/2. \quad (14c)$$

The boundary condition on n is that there be no flux of cells through the walls, thus

$$(u + V_c \bar{p}_r)n - \frac{\partial n}{\partial r} = 0 \quad \text{at } r = 0, 1/2, \quad (15a)$$

$$(v + V_c \bar{p}_z)n - \frac{\partial n}{\partial z} = 0 \quad \text{at } z = 0, \lambda. \quad (15b)$$

The initial conditions are that of a uniform state together with a small perturbation to the uniform concentration of cells:

$$\psi = 0, \quad \zeta = 0 \quad \text{and} \quad n = 1 + \varepsilon \cos(\pi r), \quad (16)$$

where $\varepsilon = 10^{-5}$. The perturbation is applied, so that the plume forms along the central axis of the cylinder.

3. Numerical Procedure

The governing eqns (8)–(10) are discretized using a conservative finite-difference scheme (Ghorai, 1997) on a staggered mesh with the stream function and vorticity stored on one set of nodes and the concentration stored on another set of nodes. The grid is chosen so that the concentration nodes lie in the interior only, whereas those of the stream function and vorticity lie in the interior and also on the boundary of the domain. The advantage of the staggered mesh is that the no-cell flux boundary condition can be satisfied immediately when discretized, without further approximation. We know that a plume is concentrated along the central axis and that there are boundary layers at the top and bottom walls due to the large cell concentration and the presence of the rigid wall, respectively. In order to resolve these gradients accurately, a non-uniform coordinate mesh is used. The transformations proposed by Roberts (1970) are taken to transform a non-uniform mesh to a uniform mesh.

An expression for the vorticity boundary condition can be obtained by expanding the stream function near the bottom surface using a three-term Taylor series expansion and by

making use of no-slip condition:

$$\zeta_w = -\frac{\zeta_{nw}}{2} - 3.0\frac{\psi_{nw}}{r_w\,(\Delta n)^2}, \tag{17}$$

where ψ_{nw}, ζ_{nw} are the values of ψ, ζ at the near-wall node (adjacent to the wall), r_w is the radial distance and Δn is the non-dimensional distance of the near-wall node from the wall.

An implicit scheme with Euler backward differencing in time and central differencing in space is used to obtain the transient solutions. A line-by-line tridiagonal matrix algorithm with relaxation is used to solve the nonlinear discretized equations. Usually an overrelaxation and an underrelaxation are used for the discretized stream function and vorticity equations, respectively. For the concentration equations, the type of relaxation depends on the parameter values. The iteration in the implicit scheme at a fixed time is terminated based on the tolerances in the vorticity and concentration. For this let

$$Tol_\zeta^k = \max_{i,j}\left|\zeta_{i,j}^k - \zeta_{i,j}^{k-1}\right|$$

and

$$Tol_n^k = \max_{i,j}\left|n_{i,j}^k - n_{i,j}^{k-1}\right|,$$

where k denotes the iteration count and i,j vary over the grid points. If Tol_ζ^k and Tol_n^k are less than the prescribed tolerances, then iteration is terminated and the same process is repeated for the next time step. The term due to time discretization is inversely proportional to time step Δt and it increases the magnitude of the diagonal entries. Thus, the tridiagonal matrices become diagonally dominant for small values of Δt. A diagonally dominant tridiagonal matrix has good convergence properties. The numerical scheme converges for the experiments reported in this paper.

Some of the results were run with different numbers of grid points to check the grid independence of the solutions. If the swimming speed is zero then the equations of bioconvection are similar to those of the heat convection problem. To validate the code, written in terms of stretched coordinates, the code has been run for the axisymmetric heat convection problem. The computed results are compared with those of Liang *et al.* (1969) and Jones *et al.* (1976) and the agreement with their results is good.

4. Results

Equations (8)–(10) possess a static solution with $\psi = \zeta = 0$ and an equilibrium exponential concentration profile

$$n_p(z) = \frac{V_c\,\lambda\exp(V_c\,z)}{\exp(V_c\,\lambda) - 1}. \tag{18}$$

If the governing parameters are above the critical values, the concentration profile develops from the initially uniform state towards eqn (18), but bioconvection begins before the profile develops fully. In the following discussions, we consider physically relevant parameter values based on a chamber diameter of approximately 0.5 cm using data from Table 1.

4.1. EFFECT OF THE ASPECT RATIO

To study the effect of the depth on plume formation, the governing parameters R, S_c, G, V_c are kept constant at

$$R = 500,\ S_c = 20,\ G = 0.01,\ V_c = 10, \tag{19}$$

and the aspect ratio is varied from small to large values. The same parameter values were used for two-dimensional bioconvection (Ghorai & Hill, 1999) with the same width of approximately 0.25 cm for a convection cell.

Since the governing parameters are above the critical values, the concentration profile initially develops towards eqn (18), but bioconvection begins before the profile develops fully. Figure 1 shows an example of the initial evolution of cell concentration in the vertical z-direction with time and also the solution given by eqn (18). At $t = 0$, the concentration is uniform and $n = 1$ approximately. As time increases, the concentration profile tends to the exponential profile given by eqn (18). Since the parameters are above the critical values, a plume begins to form (the solution becomes function of r also) at the top along the central axis before the equilibrium exponential profile is achieved.

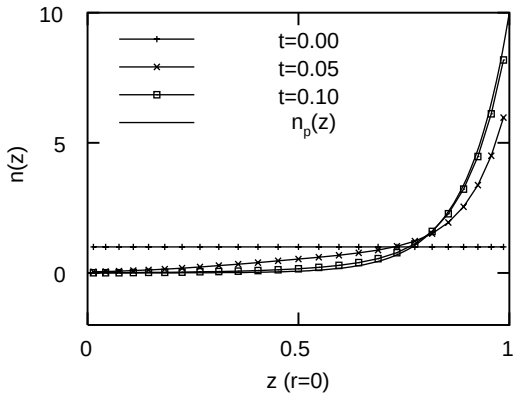

FIG. 1. Evolution of the cell concentration, $n(z)$, in the axis of the cylinder, for an ultimately unstable suspension at an early stage for $\lambda = 1$. The values of the other parameters are given in eqn (19), and $n_p(z)$ is the static equilibrium profile.

Figure 2 shows the evolution of the plume at various times from the uniform state. In this figure, we have plotted the contours of the cell concentration. Figure 2(a) shows a plume developing along the axis of the cylinder and beginning to descend [Fig. 2(b)]. The plume has hit the bottom of the cylinder at $t \approx 0.6$. The plume becomes almost steady at $t = 0.74$ [Fig. 2(d)], which can be seen from the variation of concentration at the mid-height (along the axis) of the chamber (Fig. 3). In Fig. 3, the large value at $t \approx 0.5$ is the concentration at the head of the plume when it passes through the mid-point. The final steady-state cell concentration and streamlines of the plume are plotted in Fig. 4. The solution is qualitatively similar to the two-dimensional results of Ghorai & Hill (1999).

For aspect ratio $\lambda = 2$, the evolution of concentration is similar to the $\lambda = 1$ case. The plume becomes steady rapidly as can be seen from the variation of the central concentration against time (see Fig. 5). The evolution of solution for $\lambda = 2$ is distinct from the two-dimensional case for the parameter values given by eqn (19). In the case of two-dimensions, a small "blob" (varicose instability) appears, only to ultimately disappear in the final steady state. As a result, the two-dimensional plume takes longer to become steady for $\lambda = 2$ than 1, for the parameter values in eqn (19). On the other hand, the axisymmetric plume becomes steady almost

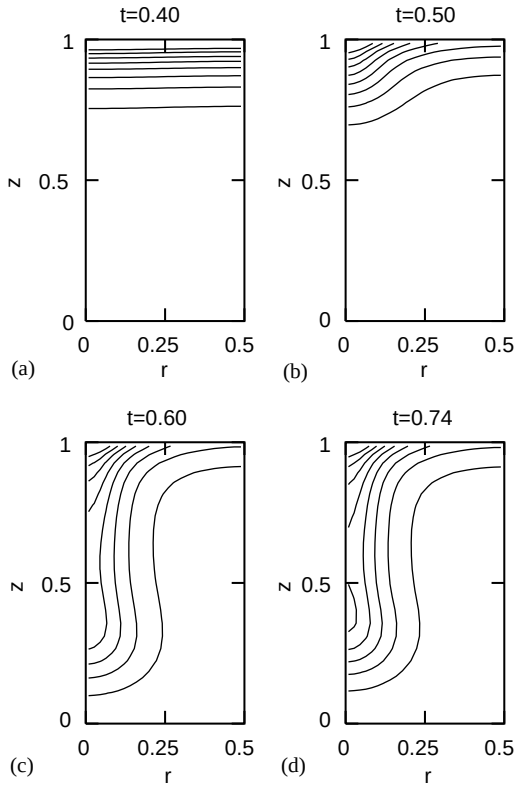

FIG. 2. Gyrotactic plume formation for the suspension shown in Fig. 1 for aspect ratio $\lambda = 1$. The concentration $n(r, z)$ at different times is plotted as contours. The contour lines take values of $0.1, 0.2, \ldots, 0.9$ of the maximum concentration n_{max}. The values of the n_{max} are 9.2, 19.6, 11.6, 12.2, respectively.

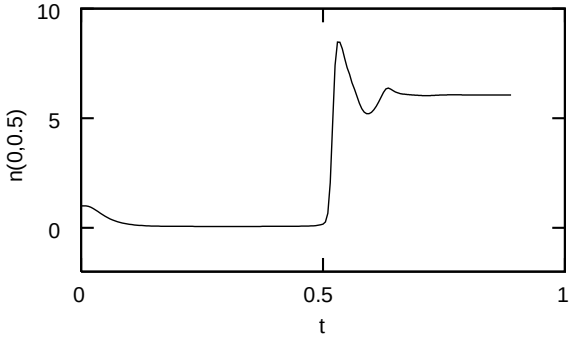

FIG. 3. Variation of concentration at the mid-height in the axis of the cylinder for aspect ratio $\lambda = 1$.

in the same time for both aspect ratios. The final steady state is plotted in Fig. 6. The solutions in the mid-region of the plume are almost independent of z, which is similar to the two-dimensional case.

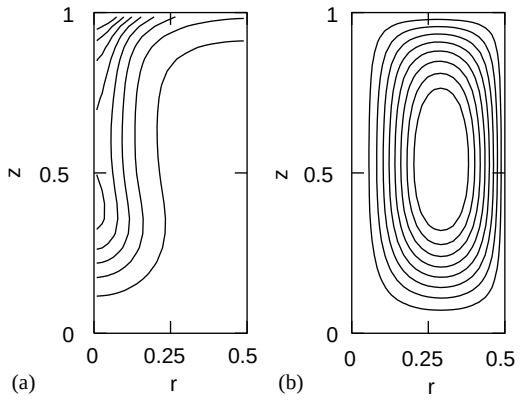

FIG. 4. Steady-state axisymmetric plume for aspect ratio $\lambda = 1$: (a) concentration and (b) streamlines. The contour levels of the concentration and stream lines are $0.1, 0.2, \ldots, 0.9$ of the maximum n ($n_{max} = 12.17$) and minimum ψ ($\psi_{min} = -0.31$) respectively.

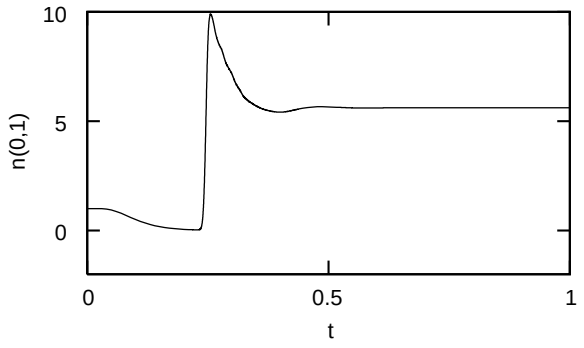

FIG. 5. Variation of concentration at the mid-height in the axis of the cylinder for aspect ratio $\lambda = 2$.

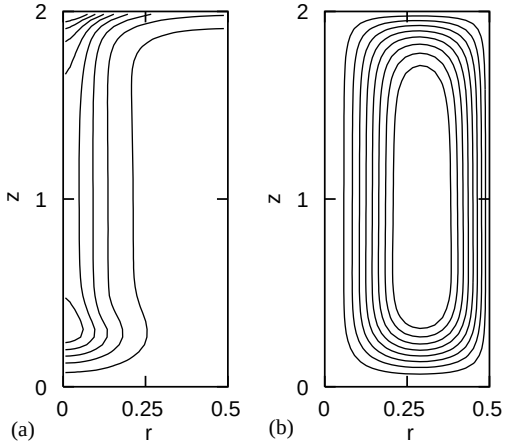

FIG. 6. Steady-state axisymmetric plume for aspect ratio $\lambda = 2$: (a) concentration and (b) streamlines. The contour levels of the concentration and stream lines are $0.1, 0.2, \ldots, 0.9$ of the maximum n ($n_{max} = 12.19$) and minimum ψ ($\psi_{min} = -0.35$) respectively.

When the aspect ratio is increased to $\lambda = 5$, the axisymmetric plume again becomes steady rapidly. In contrast in two dimensions, the solution becomes periodic with a "blob" convecting along the plume. When this blob hits the bottom of the chamber, another blob starts descending from the top of the chamber. For the axisymmetric plume, the steady-state concentration and streamlines are plotted in Fig. 7.

From Fig. 7, it is clear that the solution in the mid-region of the plume is independent of z. If the solution is independent of z, then the equations of bioconvection in the steady state simplify to

$$u = 0, \qquad v = v(r), \tag{20}$$

$$\frac{\mathrm{d}}{\mathrm{d}r}\left[\frac{1}{r}\frac{\mathrm{d}}{\mathrm{d}r}\left(r\frac{\mathrm{d}v}{\mathrm{d}r}\right)\right] = R\frac{\mathrm{d}n}{\mathrm{d}r} \tag{21}$$

and

$$\frac{\mathrm{d}n}{\mathrm{d}r} = V_c\,\bar{p}_r\,n \tag{22}$$

where in eqn (22), the condition of no cell flux through the side walls is used. To determine the solution of eqns (20)–(22), the additional

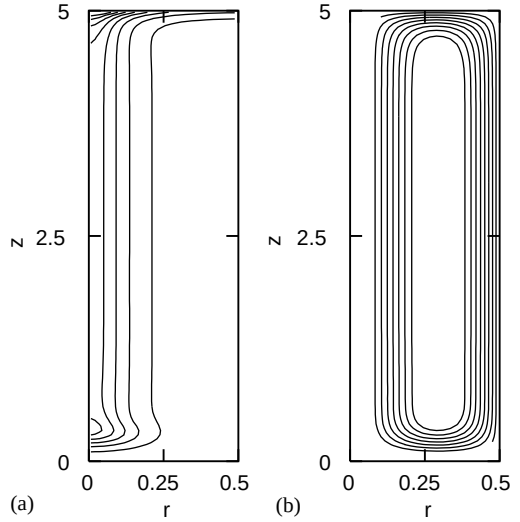

FIG. 7. Steady-state axisymmetric plume for aspect ratio $\lambda = 5$: (a) concentration and (b) streamlines. The contour levels of the concentration and stream lines are $0.1, 0.2, \ldots, 0.9$ of the maximum n ($n_{max} = 13.41$) and minimum ψ ($\psi_{min} = -0.34$), respectively.

boundary conditions are

$$\frac{dv}{dr} = 0 \quad \text{at } r = 0,\ 1/2, \tag{23}$$

$$\int_0^{1/2} v(r)\, r\, dr = 0 \tag{24}$$

and

$$\int_0^{1/2} [v(r) + V_c\, \bar{p}_z]\, n(r)\, r\, dr = 0. \tag{25}$$

Equation (23) is due to stress-free side walls, and eqns (24) and (25) are due to zero fluid flux and cell flux across any cross-section. The boundary value problem given by eqns (20)–(22) and (23)–(25) can easily be solved using iteration e.g. by the Newton–Raphson method. In Fig. 8, we compare the solution obtained using the Newton–Raphson method (solid line) with the numerical solution of the axisymmetric bioconvection (data points marked by triangles) at $z = 2.5$. It shows that there is good agreement between the axial velocity $v(r, 2.5)$ and concentration $n(r, 2.5)$.

Both the evolution and final state of the plume for the set of parameter values given by eqn (19) are different from those of the two-dimensional plume. The parameter values in eqn (19) are chosen to compare the solutions of the axisymmetric problem with those of the two-dimensional problem (Ghorai & Hill, 1999). For these values, the axisymmetric solutions become steady rapidly for aspect ratio $\lambda = 1$–5. On the other hand, the solutions for the two-dimensional case become steady more slowly as λ increases from $\lambda = 1$–4. For values of λ higher than 4, the final state of the solution is periodic.

However, there are ranges of parameter values for which the evolution and final states of the plume are similar for both the axisymmetric and two-dimensional plumes. For example, we consider the following parameter values:

$$R = 300,\ S_c = 20,\ G = 0.008,\ V_c = 20. \tag{26}$$

The variation of the central concentration, for aspect ratios $\lambda = 2$ and 4, at the mid-height of the chamber is shown in Fig. 9. We see that the plume with higher aspect ratio becomes unstable more rapidly. This is due to the fact that the chamber with the smaller aspect ratio is shallower and requires a higher Rayleigh number to become unstable. In the case of $\lambda = 2$, a small "blob" develops which ultimately disappears in the final state. The fluctuations in the concentration in Fig. 9 are due to the passing of the blobs through the mid-height of the chamber. For $\lambda = 4$, the blobs convect along the plume periodically. Thus for the parameter values given by eqn (26), the evolution of the plume from the initial uniform state is similar to the two-dimensional case.

In the numerical experiments, the width of the chamber was kept fixed and the aspect ratio λ was varied from small to large values. The number of horizontal intervals was kept fixed at 26, and the numbers of vertical intervals taken were 26, 46, 64 and 76 for aspect ratios 1, 2, 4 and 5, respectively. Some of the runs (especially those

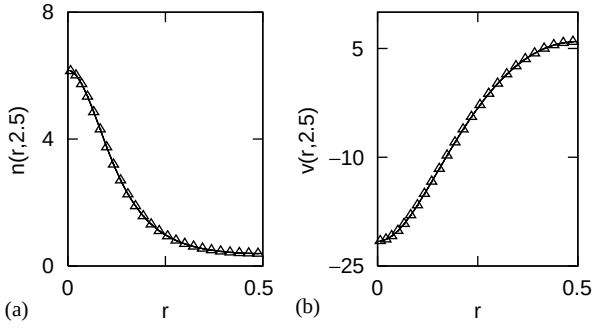

FIG. 8. Comparison between the solution of eqns (20)–(25) (solid line) and the numerical axisymmetric bioconvection problem (triangles) at $z = 2.5$.

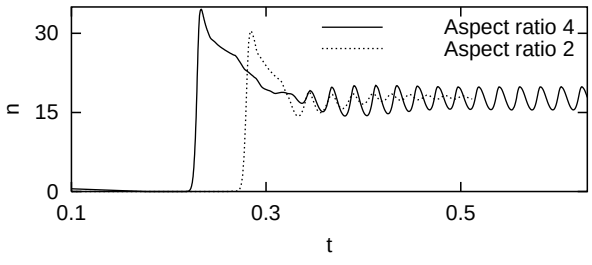

FIG. 9. Variation of concentration at the mid-height in the axis of the cylinder for two different values of aspect ratio λ. The parameter values are given by eqn (26).

with periodic blob convection) were run with finer mesh sizes to check their accuracy.

4.2. EFFECTS OF THE PARAMETER VALUES

In this section, we investigate the dependence of the final state of the plume on the gyrotaxis number, G, and the cell swimming speed, V_c, for a large aspect ratio $\lambda = 6$ of the chamber. We fix the following parameter values:

$$R = 250, \quad S_c = 20 \quad \text{and} \quad \lambda = 6. \qquad (27)$$

The parameter values given by eqn (27) are derived from a cell swimming diffusion coefficient $D = 5 \times 10^{-4}\,\text{cm}^2\,\text{s}^{-1}$ and a chamber diameter $L = 0.5\,\text{cm}$ (see Table 1). The value of $G = B\,D/L^2$ based on $B = 3.4\,\text{s}$ (Pedley & Kessler, 1992) is approximately 7×10^{-3}. The value of $V_c = W_c\,L/D$ based on $W_c = 10^{-2}\,\text{cm}\,\text{s}^{-1}$ is 10. Thus, we vary G from 2×10^{-3} to 1.1×10^{-2} and V_c from 5 to 20 to cover a range of physically relevant values. The initial conditions are given by eqn (16). The solutions tend to the final steady state rapidly for some parameter values and slowly for the others.

We consider four representative values of both the V_c and G. The values of V_c are 5, 10, 15 and 20. The values 0.002, 0.005, 0.008 and 0.011 are chosen for G. We fix a value of one parameter, say V_c, and G is varied over the above values. The details of the calculations are presented for the case $V_c = 15$.

The variation of the concentration at a point on the central axis of the plume is shown in Fig. 10. Since the length of the plume is not same

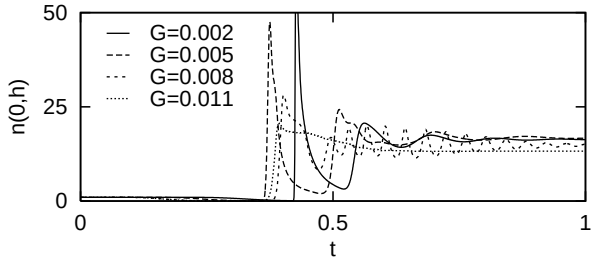

FIG. 10. Variation of concentration at height h in the axis of the cylinder for different values of G. The aspect ratio is 6 and the value of h is different for different values of G.

(see below) for the four values of gyrotaxis number, the point on the central axis is taken at different heights for different values of G. It shows that for a fixed value of V_c, the time to reach the instability stage decreases with an increase in the value of G. The fluctuation in the concentration values are appearance of "blobs" (varicose instability), which disappear leading to the final steady state. The amplitude of the fluctuations diminishes for the highest value of G.

The steady states of the plumes for different values of G are shown in Fig. 11. As the value of the gyrotaxis number G increases, the concentration along the central axis increases and concentration at the top decreases. This is for the following reason. Higher values of G increase the effect of gyrotaxis which causes more cells to focus along the axis of the cylinder. This in turn leads to more vigorous downwelling along the axis and draws more cells from the top of the chamber. The combined effect of cell swimming and gyrotaxis is weaker for smaller values of G and in such cases the plumes extend only to a fraction of the chamber's depth.

Now, we consider the results for the two-dimensional case with the same parameter values. The variation of the concentration at a point is shown in Fig. 12. The time to reach the instability stage decreases with an increase in the value of G, which is similar to the axisymmetric case. The fluctuations in the concentration values are appearance of "blobs" (varicose instability), which ultimately disappear leading to the final steady state for $G = 0.002$ and 0.005. On the other hand, they remain for $G = 0.008$ and 0.011, leading to periodic solutions. The amplitude of the fluctuations diminishes for the highest value of G.

Snapshots of the plumes for different values of G are shown in Fig. 13. As the value of gyrotaxis number G increases, the concentration along the central axis increases and concentration at the top decreases. This is similar to the axisymmetric case. On the other hand, the final states of the plume for $G = 0.008$ and 0.011 are periodic, but these are steady for the axisymmetric case. Thus, the final states of the plume are steady in axisymmetric case, but these are either steady or periodic in two dimensions for the values of G considered when $V_c = 15$.

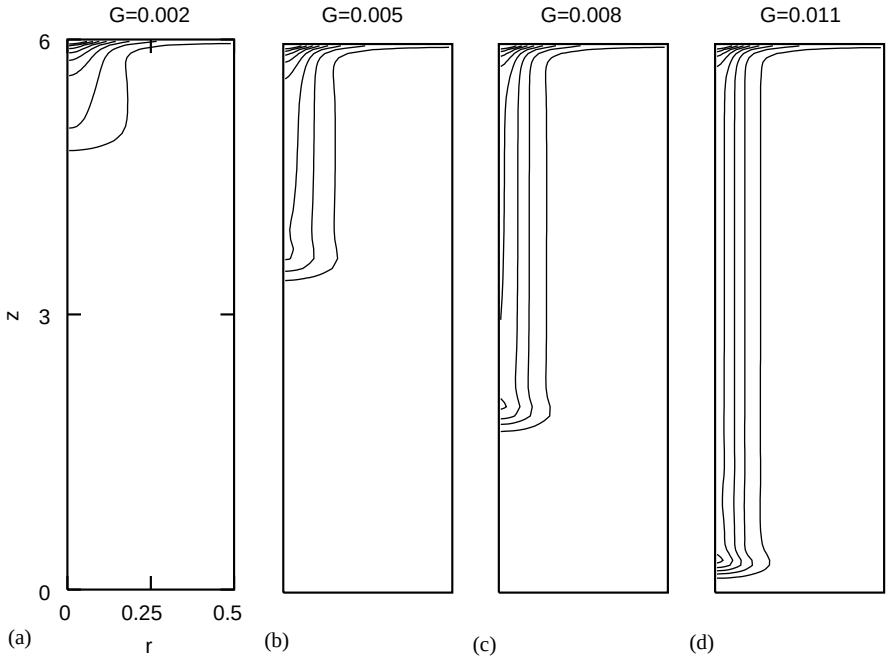

FIG. 11. Snapshots of concentrations for $V_c = 15$ for the axisymmetric case. The contour lines take values of $0.1, 0.2, \ldots, 0.8$ of the maximum concentration n_{max}. The values of n_{max} are 84.0, 53.0, 38.0 and 30.0, respectively. All the solutions are steady.

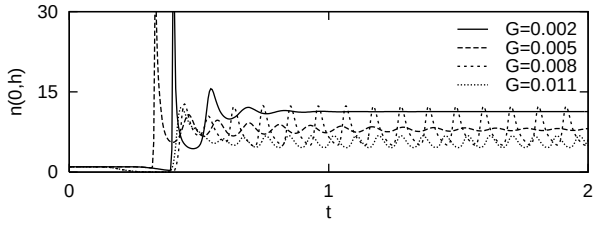

FIG. 12. Variation of concentration at height h in the two-dimensional case for different values of G. The aspect ratio is 6 and the value of h is different for different values of G.

For the other values of V_c, we summarize the results in Table 2. The plume extends to a fraction of the chamber depth for the smaller values of G or V_c, but it extends to the full depth of the chamber for larger values of both the G and V_c. From Table 2, it is clear that axisymmetric solutions are periodic only for $G = 0.011$ and $V_c = 15$, whereas two-dimensional solutions are periodic for a greater number of G and V_c values. At the highest values of $G = 0.011$ and $V_c = 20$, the solutions again become steady and the concentration at the bottom of the chamber becomes large for both the axisymmetric and two-dimensional case. Similar behaviour was observed for other parameter values (not listed) too.

For $G = 0.011$ and $V_c = 20$, the plume extends to the full depth of the chamber and the bottom boundary layer becomes strong. For these values of G and V_c, a 32×86 mesh was used in the horizontal and vertical directions. In all the other cases, a 32×76 mesh was used in the numerical experiments. Solutions for $G = 0.008$, $V_c = 20$ and $\lambda = 6$ were tested on 26×56, 26×66 and 46×76 meshes and the results were in agreement with each other.

5. A Case Study

In this section, we take the parameter values for which both the axisymmetric and two-dimensional calculations give periodic solutions and then we compare the numerical results with the observational data. The parameter values chosen are

$$S_c = 20, \quad R = 400, \quad G = 8 \times 10^{-3}, \quad V_c = 20 \quad \text{and} \quad \lambda = 6. \tag{28}$$

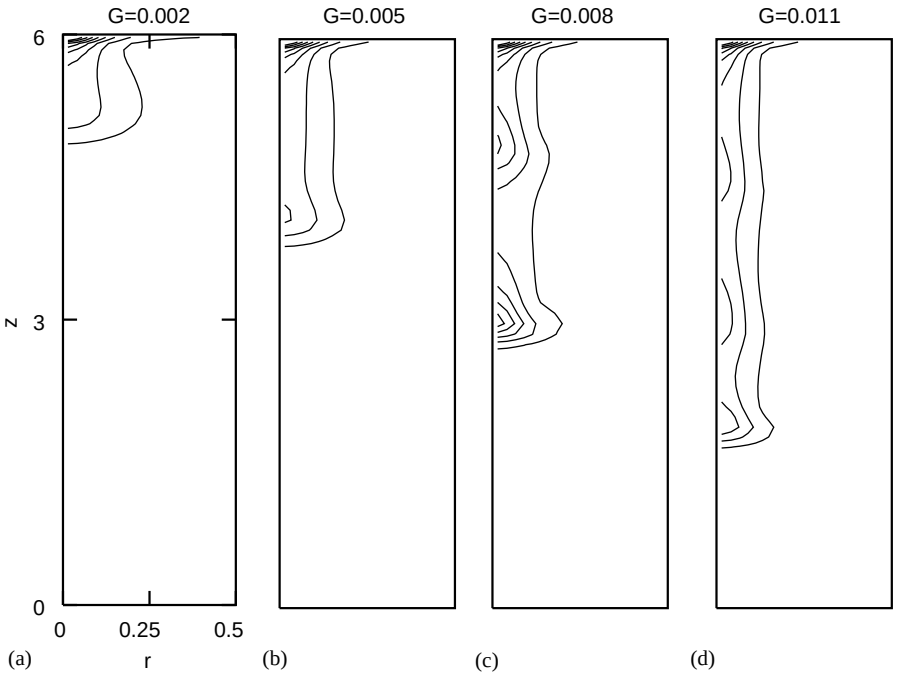

FIG. 13. Snapshots of concentrations for $V_c = 15$ for the two-dimensional case. The contour lines take values of $0.1, 0.2, \ldots, 0.8$ of the maximum concentration n_{max}. The values of n_{max} are 43.0, 30.0, 22.0 and 18.0, respectively. The solutions shown in (a) and (b) are steady while in (c) and (d) are periodic.

TABLE 2

Summary of results for the variation of G and V_c. Here, A_s and A_p denote, respectively, the steady and periodic solutions for the axisymmetric problem. Similar notations, T_s and T_p, are used for the two-dimensional case

	V_c			
G	5	10	15	20
0.002	A_s/T_s	A_s/T_s	A_s/T_s	A_s/T_s
0.005	A_s/T_s	A_s/T_s	A_s/T_s	A_s/T_p
0.008	A_s/T_s	A_s/T_s	A_s/T_p	A_s/T_p
0.011	A_s/T_s	A_s/T_p	A_p/T_p	A_s/T_s

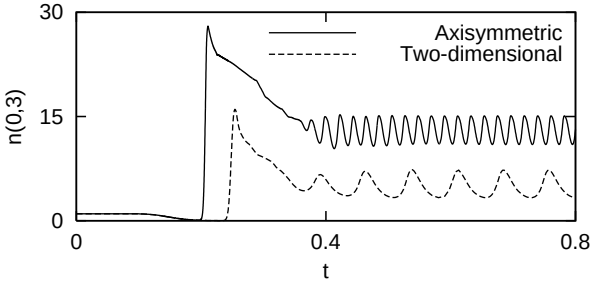

FIG. 14. Variation of the central concentration for axisymmetric and two-dimensional bioconvection. The parameter values are given by eqn (28).

The parameter values in eqn (28) are based on a chamber approximately 1 cm wide. In the numerical experiments, 32×96 meshes were used in the axisymmetric and two-dimensional calculations.

The variation of the central concentration at the mid-height of the chamber against time is shown in Fig. 14. Both the two-dimensional and axisymmetric solutions are periodic. The periods of oscillation are approximately 0.02 and 0.08 (in non-dimensional units) for the axisymmetric and two-dimensional bioconvection, respectively. Assuming that the diffusion coefficient $D = 5 \times 10^{-4}\,\mathrm{cm^2\,s^{-1}}$ and the width $L = 1$ cm, the time-scale for the flow is $L^2/D = 2 \times 10^3$ s. Thus, in dimensional terms, the periods are 40 s and 2 min 40 s for the axisymmetric and two-dimensional bioconvection, respectively.

Snapshots of the periodic solutions for the two cases are shown in Fig. 15. In both cases, two blobs are descending along the plume. The formation of each blob takes place nearer to

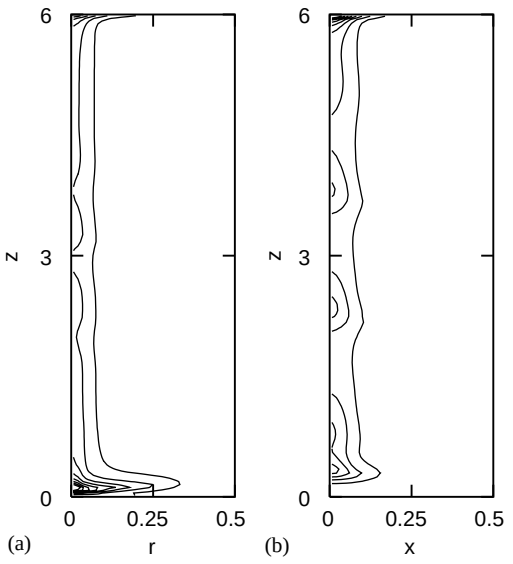

FIG. 15. Snapshots of the concentration at $t = 0.8$ for the (a) axisymmetric and (b) two-dimensional bioconvection, respectively. The parameter values are given by eqn (28). The contour levels of the concentration are $0.1, 0.2, \ldots, 0.8$ of the maximum concentration. The maximum concentrations are approximately 58 and 22 for the axisymmetric and two-dimensional bioconvection, respectively.

the top of the plume in two dimensions. As a result, the wavelength of the varicose mode is approximately 1 and 1.4 (in non-dimensional units) for the axisymmetric and two-dimensional bioconvection, respectively. Since the diameter is approximately 1 cm, the dimensional wavelengths are approximately 1 and 1.4 cm.

Some observational data were given by Kessler (1986) for gyrotactic focussing in a cylinder of diameter 1.3 cm. Initially, the cells were focussed by imposing a downward Poiseuille flow of 0.1 cm s^{-1}. Then the imposed flow was stopped and the axial downward flow was sustained by gyrotaxis. The distances between the blobs were in the range 1.5–2 cm (see Fig. 4 in Kessler, 1986). The central flow speed u_0 in a self-sustained gyrotactic flow is approximately 1–1.5 times the speed W_c of the cell. Since the blobs are heavier, they sink with speed $2u_0$–$5u_0$ (Kessler, 1986). Based on the distance 1.5–2 cm and sinking velocity $2u_0$–$5u_0$, the observed periods of oscillation are approximately 20–100 s. The numerically calculated values of the periods are 40 s and 2 min 40 s for the axisymmetric and two-dimensional bioconvection, respectively. Thus, for the parameter values given by eqn (28), the period of oscillation for the axisymmetric case is much smaller than that of two-dimensional case and is nearer to the observational data. The wavelengths of the varicose mode (i.e. distance between the blobs) are close to observational data for both cases.

6. Conclusion

In the case of axisymmetric bioconvection, we have seen two different states of the plume: either steady or periodic. For axisymmetric bioconvection, the plume becomes unsteady via *varicose* instability. The other possible *meandering* instability (seen in two-dimensional bioconvection) does not appear due to the imposed axisymmetry. Thus, to see the effect of *meandering* type instability, we should consider solutions which are functions of (r, ϕ, z), i.e. full three-dimensional numerical simulations.

The effect of changing the aspect ratio has been investigated by increasing the value of λ from small to large values. One set of fixed parameter values is the same as in the two-dimensional case (Ghorai & Hill, 1999). When $\lambda \geqslant 5$, the final state of the plume is always steady for any value of λ for axisymmetric bioconvection, but periodic in the two-dimensional case. The evolution of the plume for another set of parameter values is similar to the two-dimensional case. When the solution is steady, the solution in the mid-region of the plume is independent of the vertical coordinate z.

The effects of the G and V_c on the plume solution are investigated for a range of physically relevant parameter values. When the values of either G or V_c are small, the plumes do not extend to the bottom of the chamber. The varicose instability occurs in most of the runs. The blobs disappear in certain cases leading to steady states, or they remain in the final state in other cases. As V_c increases from small to large values and G takes small to moderate values, the duration of varicose instability increases, but when G is much larger, the varicose instability almost disappears.

Detailed comparisons between axisymmetric and two-dimensional bioconvection have been made. It was found that for the set of parameter

values considered, the time period of the varicose oscillation in axisymmetric bioconvection is more realistic and smaller than that of the two-dimensional bioconvection. The wavelengths of the varicose mode are comparable for both the axisymmetric and two-dimensional simulations, and close to the experimental observations. Similar results for the period and wavelengths of the varicose mode have been observed in other runs with different sets of parameter values. The range of parameter values, for which the final states of the plume are periodic, is much smaller than in the two-dimensional case.

REFERENCES

Ghorai, S. (1997). Bioconvection and plumes. Ph.D. Thesis, University of Leeds.

Ghorai, S. & Hill, N. A. (1999). Development and stability of gyrotactic plumes in bioconvection. *J. Fluid Mech.* **400,** 1–31.

Ghorai, S. & Hill, N. A. (2000a). Periodic arrays of gyrotactic plumes in bioconvection. *Phys. Fluids* **12,** 5–22.

Ghorai, S. & Hill, N. A. (2000b). Wavelengths of gyrotactic plumes in bioconvection. *Bull. Math. Biol.* **62,** 429–450.

Harashima, A., Watanabe, M. & Fujishiro, I. (1988). Evolution of bioconvection patterns in a culture of motile flagellates. *Phys. Fluids* **31,** 764–775.

Hinch, E. J. & Leal, L. J. (1972). The effect of Brownian motion on the rheological properties of a suspension of non-spherical particles. *J. Fluid Mech.* **52,** 683–712.

Hopkins, M. M. & Fauci, L. J. (2002) A computational model of the collective fluid dynamics of motile micro-organisms. *J. Fluid Mech.* **455,** 149–174.

Jones, C. A., Moore, D. R. & Weiss, N. O. (1976). Axisymmetric convection in a cylinder. *J. Fluid Mech.* **73,** 353–388.

Kessler, J. O. (1985). Hydrodynamic focusing of motile algal cells. *Nature* **313,** 218–220.

Kessler, J. O. (1986). Individual and collective fluid dynamics of swimming cells. *J. Fluid Mech.* **173,** 191–205.

Liang, S. F., Vidal, A. & Acrivos, A. (1969). Buoyancy-driven convection in cylindrical geometries. *J. Fluid Mech.* **36,** 239–256.

Pedley, T. J. Hill, N. A. & Kessler, J. O. (1988). The growth of bioconvection patterns in a uniform suspension of gyrotactic microorganisms. *J. Fluid Mech.* **195,** 223–238.

Pedley, T. J. & Kessler, J. O. (1992). Hydrodynamic phenomena in suspensions of swimming microorganisms. *Ann. Rev. Fluid Mech.* **24,** 313–358.

Lord Rayleigh (1916). On convection currents in a horizontal layer of fluid, when the higher temperature is on the under side. *Philos. Mag.* **32,** 529–546.

Roberts, G. O. (1970). Computational meshes for boundary layer problems. In: *Second International Conference on Numerical Methods in Fluid Dynamics* (Holt, M., ed.), Lecture Notes in Physics, Vol. 8, pp. 175–184, New York: Academic Press.

Appendix

Validation of Axisymmetric Code

If the cell swimming speed is zero, then the form of the equations of bioconvection reduces to that of the thermal convection. Thus, the axisymmetric bioconvection code, written in stretched coordinates has been run for the thermal convection problem. The computed results are compared with those of Liang *et al.* (1969) and Jones *et al.* (1976).

The grid is staggered, with the nodes for the stream function and vorticity lying on one set of points and that of temperature on another set. The grid geometry is modified slightly (from that used in bioconvection) to incorporate the boundary conditions into the discretized equations. Thus, the nodes for the temperature lie laterally only in the interior, but vertically in both the interior and on the boundary. The details of the comparisons are given separately.

Appendix A

Comparison with Liang *et al.*

In terms of the dimensionless stream function ψ, the vorticity ζ and the temperature θ, the following equations are obtained:

$$-\zeta = \frac{1}{r}\frac{\partial^2\psi}{\partial z^2} + \frac{\partial}{\partial r}\left(\frac{1}{r}\frac{\partial\psi}{\partial r}\right), \tag{A.1}$$

$$\frac{\partial}{\partial r}(u\zeta) + \frac{\partial}{\partial z}(w\zeta) = -\frac{R}{P}\frac{\partial\theta}{\partial r} + \left[\frac{\partial}{\partial r}\left(\frac{1}{r}\frac{\partial}{\partial r}(r\zeta)\right) + \frac{\partial^2\zeta}{\partial z^2}\right], \tag{A.2}$$

$$\frac{1}{r}\frac{\partial}{\partial r}\left[r\left(u\theta - \frac{\partial\theta}{\partial r}\right)\right] + \frac{\partial}{\partial z}\left[w\theta - \frac{\partial\theta}{\partial z}\right] = 0, \tag{A.3}$$

where P and R are the Prandtl and Rayleigh numbers, respectively. The lateral surface is insulated (i.e. no flux of heat at $r = 1$) and is assumed to be stress free. The top and bottom surfaces are either stress free or rigid, and

$$\theta = 1 \quad \text{at } z = 0 \quad \text{and} \quad \theta = 0 \quad \text{at } z = 1.$$

The average Nusselt numbers, $\bar{N}_0$ and $\bar{N}_1$, are defined by

$$N_{0,1} = 2\int_0^1 r \left|\frac{\partial\theta}{\partial z}\right|_{z=0,1} \mathrm{d}r,$$

which due to energy conservation, should be identical when the top and bottom surfaces are either both rigid or stress free. In Liang *et al.* (1969), the equations are formulated in non-conservative form and, consequently, the computed values of $\bar{N}_0$ and $\bar{N}_1$ are not identical but lie within 1% of one another. Here, we use the conservative form of the eqns (A.1)–(A.3), and hence $\bar{N}_0$ and $\bar{N}_1$ are always equal.

The properties of the solutions are compared with the numerical solutions of Liang *et al.* in Table A1. We only compare the solutions for constant viscosity (run nos. 3, 9 and 13 of Liang *et al.*). In Table A1, the results in Roman font correspond to the solution of Liang *et al.* (1969) and those in italics are the solutions using the modified bioconvection code. The lower boundary is solid. The quantities presented are the maximum value of stream function $|\psi|_{max}$ and $\bar{N} = \frac{1}{2}(\bar{N}_0 + \bar{N}_1)$.

The solutions obtained using the modified bioconvection code are in good agreement with the results of Liang *et al.* (1969). Figure A1 shows the contours of streamlines and isotherms

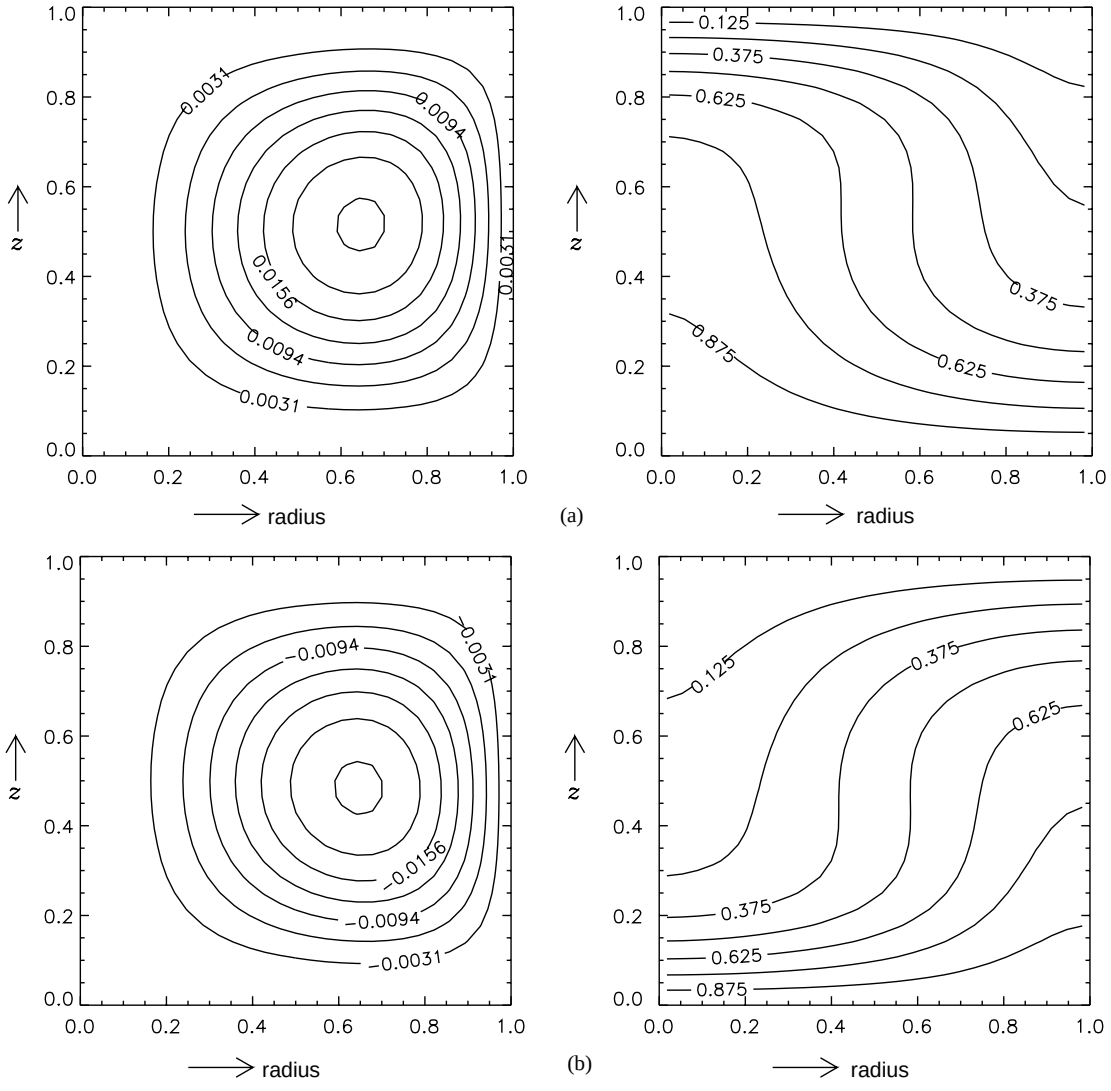

FIG. A1. Streamlines and isotherms (a) upflow at the centre (b) downflow at the centre for the thermal convection problem solved using the modified bioconvection code.

TABLE A1
Comparison between the numerical results of Liang et al. (roman font) and of the modified bioconvection code (italics)

Mesh	Upper		R	P	$\|\psi\|_{max}$		$\bar{N}$	
	Solid	Free			Upflow at centre	Downflow at centre	Upflow at centre	Downflow at centre
29×29	×	—	4000	100	0.0225	0.0225	1.836	1.836
					0.0225	*0.0225*	*1.843*	*1.843*
19×19	×	—	4000	1	2.151	2.136	1.784	1.777
					2.156	*2.156*	*1.799*	*1.799*
29×29	—	×	4000	100	0.0310	0.0322	2.353	2.414
					0.0308	*0.0317*	*2.329*	*2.381*

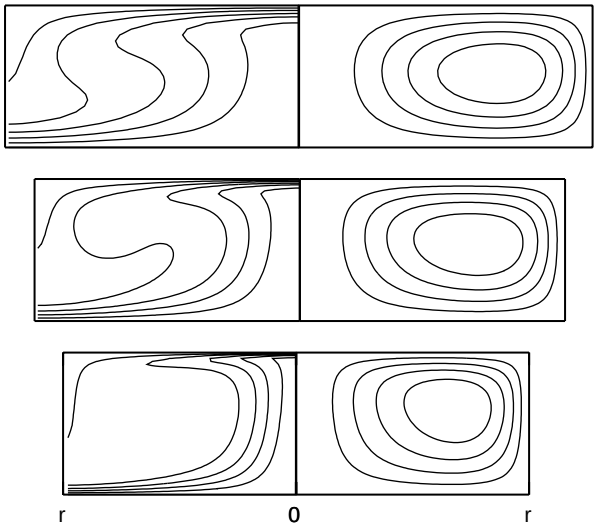

FIG. B1. Isotherms and streamlines profiles for $P_r = 6.8$ and $R = 6R_c$, $20R_c$ and $100R_c$. The contour lines are equally spaced. The mesh sizes (vertical × horizontal) for the numerical experiments are, respectively, 24×42, 48×74 and 48×56. The non-dimensional height is 1.

for the first set of runs i.e. $R = 4000$, $P = 100$ with solid top and bottom surfaces.

Appendix B

Comparison with Jones *et al.*

Axisymmetric Rayleigh–Beńard convection of a Boussinesq fluid was also investigated by Jones *et al.* (1976), who studied the effect of Prandtl number on heat flux. In terms of the dimensionless stream function ψ, the vorticity ζ and the temperature θ, the following equations are obtained:

TABLE B1
Nusselt number N as a function of the Rayleigh number R and dimensionless radius λ. Comparison between the numerical results of Jones et al. (third column) and of the modified bioconvection code (fourth column)

R	λ	N	N
$6R_c$	1.75	3.48	3.49
$20R_c$	1.54	5.31	5.31
$100R_c$	1.17	8.89	8.89

$$-\zeta = \frac{1}{r}\frac{\partial^2\psi}{\partial z^2} + \frac{\partial}{\partial r}\left(\frac{1}{r}\frac{\partial\psi}{\partial r}\right), \tag{B.1}$$

$$\frac{\partial\zeta}{\partial t} + \frac{\partial}{\partial r}(u\zeta) + \frac{\partial}{\partial z}(w\zeta) = -R\,P_r\frac{\partial\theta}{\partial r} + P_r\left[\frac{\partial}{\partial r}\left(\frac{1}{r}\frac{\partial}{\partial r}(r\zeta)\right) + \frac{\partial^2\zeta}{\partial z^2}\right] \tag{B.2}$$

$$\frac{\partial\theta}{\partial t} + \frac{1}{r}\frac{\partial}{\partial r}\left[r\left(u\theta - \frac{\partial\theta}{\partial r}\right)\right] + \frac{\partial}{\partial z}\left[w\theta - \frac{\partial\theta}{\partial z}\right] = 0, \tag{B.3}$$

where P_r and R are the Prandtl and Rayleigh numbers, respectively. The lateral surface is insulated (i.e. no flux of heat) and is assumed to be stress free. The top and bottom surfaces are stress free and

$$\theta = 1 \quad \text{at } z = 0 \quad \text{and} \quad \theta = 0 \quad \text{at } z = 1.$$

Linear theory predicts the onset of instability at $R = R_c = 27\pi^4/4$ with dimensionless radius $\lambda = 1.725$. The modified bioconvection code was run for the values of the Prandtl number and Rayleigh numbers shown in the caption of Fig. B1. Figure B1 is in agreement with that of Jones *et al.* (1976) (see p. 375 of the reference). The effectiveness of convection is measured by the ratio of the total heat flux to the flux that would have been carried in the absence of convection: the Nusselt number

$$N = \frac{2}{\lambda^2} \int_0^{\lambda} \left(w\,\theta - \frac{\partial \theta}{\partial z} \right) r\,\mathrm{d}r,$$

which for a steady state is a function of R, P_r and λ only. The calculated values of the Nusselt number are compared with those of Jones *et al.* (1976) in Table B1. The agreement between the results is excellent.